

## Article

# An Integrated Na<sub>2</sub>S – Electrocatalyst Nanostructured Cathode for Sodium–Sulfur Batteries at Room Temperature

Sichang Ma, Yueming Zhu, Yadong Yang, Dongyang Li, Wendong Tan, Ling Gao, Wanwei Zhao, Wenbo Liu, Wenyu Liang \* and Rui Xu \*

School of Materials Science and Engineering, University of Science and Technology Beijing, Beijing 100083, China; ma\_sichang@163.com (S.M.); amingosk@163.com (Y.Z.); 13717839375@163.com (Y.Y.); d202410297@xs.ustb.edu.cn (D.L.); tanwendong19980319@163.com (W.T.); m202210295@xs.ustb.edu.cn (L.G.); m202210415@xs.ustb.edu.cn (W.Z.); 2406394418@pku.edu.cn (W.L.)

\* Correspondence: liangw@ustb.edu.cn (W.L.); ruixu@ustb.edu.cn (R.X.)

**Abstract:** Room-temperature sodium–sulfur (RT Na–S) batteries offer a superior, high-energy-density solution for rechargeable batteries using earth-abundant materials. However, conventional RT Na–S batteries typically use sulfur as the cathode, which suffers from severe volume expansion and requires pairing with a sodium metal anode, raising significant safety concerns. Utilizing Na<sub>2</sub>S as the cathode material addresses these issues, yet challenges such as Na<sub>2</sub>S's low conductivity as well as the shuttle effect of polysulfide still hinder RT Na–S battery development. Herein, we present a simple and cost-effective method to fabricate a Na<sub>2</sub>S–Na<sub>6</sub>CoS<sub>4</sub>/Co@C cathode, wherein Na<sub>2</sub>S nanoparticles are embedded in a conductive carbon matrix and coupled with dual catalysts, Na<sub>6</sub>CoS<sub>4</sub> and Co, generated via the in situ carbothermal reduction of Na<sub>2</sub>SO<sub>4</sub> and CoSO<sub>4</sub>. This approach creates a three-dimensional porous composite cathode structure that facilitates electrolyte infiltration and forms a continuous conductive network for efficient electron transport. The in situ formed Na<sub>6</sub>CoS<sub>4</sub>/Co electrocatalysts, tightly integrated with Na<sub>2</sub>S, exhibit strong catalytic activity and robust physicochemical stabilization, thereby accelerating redox kinetics and mitigating the polysulfide shuttle effect. As a result, the Na<sub>2</sub>S–Na<sub>6</sub>CoS<sub>4</sub>/Co@C cathode achieves superior capacity retention, demonstrating a discharge capacity of 346 mAh g<sup>−1</sup> after 100 cycles. This work highlights an effective strategy for enhancing Na<sub>2</sub>S cathodes with embedded catalysts, leading to enhanced reaction kinetics and superior cycling stability.

**Keywords:** room-temperature sodium–sulfur batteries; Na<sub>2</sub>S cathode; shuttle effect; sodium polysulfides; catalysts



Academic Editor: Yong-Joon Park

Received: 1 December 2024

Revised: 23 December 2024

Accepted: 24 December 2024

Published: 27 December 2024

**Citation:** Ma, S.; Zhu, Y.; Yang, Y.; Li, D.; Tan, W.; Gao, L.; Zhao, W.; Liu, W.; Liang, W.; Xu, R. An Integrated Na<sub>2</sub>S–Electrocatalyst Nanostructured Cathode for Sodium–Sulfur Batteries at Room Temperature. *Batteries* **2025**, *11*, 9. <https://doi.org/10.3390/batteries11010009>

**Copyright:** © 2024 by the authors. Licensee MDPI, Basel, Switzerland. This article is an open access article distributed under the terms and conditions of the Creative Commons Attribution (CC BY) license (<https://creativecommons.org/licenses/by/4.0/>).

## 1. Introduction

Room temperature sodium–sulfur (RT Na–S) batteries, which store energy through the conversion reaction between elemental sulfur and sodium sulfide at the cathode, are emerging as promising candidates for next-generation energy storage systems. With a high theoretical energy density of 1274 Wh kg(S)<sup>−1</sup> and the potential for low-cost, earth-abundant electrode materials, RT Na–S batteries offer an impressive alternative for energy storage [1–3]. However, their development is still in its early stages, hindered by several intrinsic challenges, which are similar to the challenges faced by lithium–sulfur batteries, including low practical capacity, poor Coulombic efficiency, and rapid capacity fade. These issues are largely resulted from the insulating nature of sulfur, the sluggish kinetics of the Na–S system, and the shuttle effect caused by the dissolution and diffusion of high-order sodium polysulfides (NaPSs) in ether-based electrolytes during cycling [4–8].

To tackle these challenges, remarkable efforts have focused on developing conductive hosts for the sulfur cathode, often combined with catalytic materials to enhance the Na–S reactions. Catalysts can accelerate the redox reactions of NaPSs, especially under high charge and discharge current densities, while simultaneously improving the adsorption of NaPSs to mitigate their dissolution and suppress the shuttle effect [9–14]. Among various catalytic materials, cobalt (Co)-based catalysts have garnered attention due to their enhanced adsorption capabilities and active sites, which help restrain the shuttle effect and accelerate NaPS redox reactions [15–19]. For example, Zhang et al. [15] synthesized atomic cobalt-decorated hollow carbon nanospheres as a sulfur host for RT Na–S batteries, demonstrating that atomic Co could reduce  $\text{Na}_2\text{S}_4$  into  $\text{Na}_2\text{S}$  electrocatalytically, significantly alleviating polysulfide dissolution as well as improving electrochemical performance. In 2020, Qin et al. [16] incorporated polar  $\text{Co}_3\text{C}$ –Co into fluorinated carbon nanotube arrays in a 3D framework (FCNT@ $\text{Co}_3\text{C}$ –Co) to improve the conversion of NaPSs, while Yang et al. [17] developed chain-mail catalysts of porous nitrogen-doped carbon nanofibers (PCNFs) encapsulating Co nanoparticles, which enhanced sulfur conversion kinetics. Du et al. [18] proposed a “branch-leaf” CNF-L@Co/S electrode, which exhibited excellent electrochemical performance due to the unique Co–S–Na molecular layer formed on the Co surface.

Despite these advances, pairing sulfur as the cathode with metallic sodium as the anode raises significant safety concerns due to dendrite formation [20,21]. Furthermore, the sodiation of sulfur results in a large volume expansion (up to 160%) during the discharge process, resulting in electrode cracking, peeling, and the loss of active material [2,22]. One promising solution is the use of sodium sulfide ( $\text{Na}_2\text{S}$ ), the fully sodiated form of sulfur, as an alternative cathode material. Since  $\text{Na}_2\text{S}$  is already in a fully sodiated state and tends to shrink during desodiation, it circumvents the volume expansion problem associated with sulfur sodiation [23]. Additionally,  $\text{Na}_2\text{S}$  can be coupled with Na–metal-free anodes, such as hard carbon or tin (Sn), to form a complete battery [24,25]. Over the years, there have been several attempts to use  $\text{Na}_2\text{S}$  as the starting cathode material in RT Na–S batteries. In 2015, Yu and Manthiram [24] first explored  $\text{Na}_2\text{S}$  as a cathode material by injecting  $\text{Na}_2\text{S}$  powder into a slurry with multi-walled carbon nanotubes, resulting in slow kinetics of conversion due to the large particle size of  $\text{Na}_2\text{S}$ . In 2019, Wang et al. [23] improved this approach by synthesizing hollow  $\text{Na}_2\text{S}$  nanospheres embedded in a conductive carbon matrix, showing high-rate performance. Other strategies have involved  $\text{Na}_2\text{S}/\text{C}$  composites formed by the carbothermal reduction of  $\text{Na}_2\text{SO}_4$  [26,27], where Bloi et al. [26] and Geng et al. [27] developed novel  $\text{Na}_2\text{S}@C$  cathodes with improved structural and electrochemical properties. While these efforts have made significant progress in advancing  $\text{Na}_2\text{S}$  cathodes, only one study has explored the role of catalytic additives to enhance redox kinetics and alleviate the dissolution and shuttle effects of NaPSs. Gao et al. [28] developed a  $\text{Na}_2\text{S}/\text{Na}_2\text{Te}@C$  cathode, where an in situ  $\text{Na}_2\text{TeS}_3$  interface was formed, promoting ion diffusion and electron transport. This interface not only improved the utilization of active material but also mitigated the shuttle effect. This work highlights the importance of catalyst integration in  $\text{Na}_2\text{S}$  cathodes for enhancing performance and calls for further research into this strategy.

In this work, we explore the catalytic effects of Co-based electrocatalysts within  $\text{Na}_2\text{S}$  cathodes. Using a simple carbothermal reduction process with  $\text{Na}_2\text{SO}_4$  and  $\text{CoSO}_4$ , we successfully embed  $\text{Na}_2\text{S}$  nanoparticles within a carbon matrix, decorated with binary catalysts  $\text{Na}_6\text{CoS}_4$  and Co ( $\text{Na}_2\text{S}$ – $\text{Na}_6\text{CoS}_4/\text{Co}$ ). By utilizing  $\text{Na}_2\text{SO}_4$ , a stable, eco-friendly, and low-cost precursor, we streamline the production of  $\text{Na}_2\text{S}$  cathodes and reduce material costs. Through the high-temperature carbothermal reduction of the  $\text{Na}_2\text{SO}_4$ – $\text{CoSO}_4$ @PVP-KB precursor, a conductive  $\text{Na}_2\text{S}$ – $\text{Na}_6\text{CoS}_4/\text{Co}@C$  composite cathode is formed, featuring a three-dimensional porous carbon network composed of secondary particles approximately

50 nm in size. This structure enhances both electronic and ionic transport. The  $\text{Na}_6\text{CoS}_4/\text{Co}$  catalysts strongly interact with  $\text{Na}_2\text{S}$ , improving catalytic activity, accelerating redox kinetics, and mitigating the shuttle effect. Compared to conventional  $\text{Na}_2\text{S}@\text{C}$  cathodes, the  $\text{Na}_2\text{S}-\text{Na}_6\text{CoS}_4/\text{Co}@\text{C}$  composite demonstrates significantly higher discharge capacity and superior cycling performance.

## 2. Materials and Methods

### 2.1. Synthesis Methods of $\text{Na}_2\text{S}-\text{Na}_6\text{CoS}_4/\text{Co}@\text{C}$ and $\text{Na}_2\text{S}@\text{C}$

A total of 1 g of polyvinylpyrrolidone (PVP), 4 g of  $\text{Na}_2\text{SO}_4\cdot\text{H}_2\text{O}$ , 1 g of  $\text{CoSO}_4\cdot 7\text{H}_2\text{O}$ , and 1 g of Ketjen Black were added into 100 mL anhydrous ethanol and stirred for 1 h. Then, the obtained mixture was intensively ultrasonicated for 30 min to form a homogeneous suspension, and the suspension was continuously stirred for two days until ethanol was entirely evaporated. The dried sample was further ground. Then, the powder was heated at 900 °C for 3 h under a heating and cooling rates of 5 °C  $\text{min}^{-1}$  to obtain  $\text{Na}_2\text{S}-\text{Na}_6\text{CoS}_4/\text{Co}@\text{C}$ . The  $\text{Na}_2\text{S}@\text{C}$  was synthesized by a similar process as for  $\text{Na}_2\text{S}-\text{Na}_6\text{CoS}_4/\text{Co}@\text{C}$  except with the absence of  $\text{CoSO}_4\cdot 7\text{H}_2\text{O}$ .

### 2.2. Electrode Preparations and Electrochemical Performance Measurements

For cathode, the slurry was prepared by mixing active materials ( $\text{Na}_2\text{S}-\text{Na}_6\text{CoS}_4/\text{Co}@\text{C}$  or  $\text{Na}_2\text{S}@\text{C}$ ), Super P, and PVP binder in the weight ratio of 8:1:1 in NMP. After which, the uniform slurry was cast onto a carbon-coated aluminum foil and then dried under ambient temperature for 48 h to remove the solvent. The electrodes were then punched into disc in 12 mm diameters, and the mass loadings of  $\text{Na}_2\text{S}$  and  $\text{Na}_2\text{S}-\text{Na}_6\text{CoS}_4/\text{Co}$  in the cathode were around 0.45–0.50  $\text{mg cm}^{-2}$ . CR2032-type coin cells were assembled with as-synthesized cathode, commercial Na foil anode and separator (Celgard 2500) with the addition of 30  $\mu\text{L}$  electrolyte, consisting of 1 M  $\text{NaCF}_3\text{SO}_3$  in DIGLYME solvent with 5 wt% fluoroethylene carbonate (FEC) as additive. The diameter of Na foil is 14 mm and the diameter of Celgard 2500 separator is 18 mm. All the experiments mentioned were conducted in a glovebox with oxygen and water contents of less than 0.1 ppm. Electrochemical performance of the coin cells was investigated on NEWARE within the voltage window of 0.5–3.0 V (vs.  $\text{Na}/\text{Na}^+$ ). The specific capacity of Na-S batteries was calculated in accordance with the mass of the sulfur content in the cathode. Cyclic voltammetry was performed using a CHI 660E electrochemical workstation at a scan rate of 0.1  $\text{mV s}^{-1}$  between 0.5 and 3.0 V. The electrochemical impedance spectroscopy (EIS) measurements were conducted on a Biologic VMP-3 electrochemical workstation.

### 2.3. Characterizations

$\text{Cu K}\alpha$  radiation was applied for X-ray diffraction (XRD) measurement within the range of 10°–90° (D/MAX 2500, Rigaku, Tokyo, Japan). Chemical structures were characterized by using a Raman spectroscopy (Thermo Scientific (Waltham, MA, USA) DXR,  $\lambda = 532$  nm). The morphology was investigated with a field emission scanning electron microscope (FESEM, ZeissSigma-300, Oberkochen, Germany) equipped with energy-dispersive X-ray spectroscopy (EDS). In addition, a transmission electron microscope (JEM-2200FS JEOL, Tokyo, Japan) was used to acquire HRTEM images. TG analyses were conducted on a HITACHI STA200 (Tokyo, Japan) analyzer to measure the thermal decomposition behavior of samples in the temperature range of 30 °C to 600 °C under the heating rate of 10 °C  $\text{min}^{-1}$  under dry air. X-ray photoelectron spectroscopy (XPS) data were collected with a Thermo Scientific K-Alpha X-ray photoelectron spectroscopy. The spectra were obtained with a monochromatic Al  $\text{K}\alpha$  source (1486.6 eV) at 12 kV, 6 mA. Nitrogen adsorption–desorption measurements were carried out by a Micromeritics ASAP

2020 system, and the Brunauer–Emmett–Teller (BET) and Barrett–Joyner–Halenda (BJH) methods were employed to calculate the specific surface areas and pore size distributions, respectively.

#### 2.4. $\text{Na}_2\text{S}_6$ Visualized Adsorption Experiments

The  $\text{Na}_2\text{S}_6$  solution containing  $\text{Na}_6\text{CoS}_4/\text{Co}@C$  or  $C$  was fabricated by dispersing  $\text{Na}_2\text{S}-\text{Na}_6\text{CoS}_4/\text{Co}@C$  or  $\text{Na}_2\text{S}@C$  and  $S$  (molar ratio 1:5) into DIGLYME at  $60^\circ\text{C}$  under intense agitation overnight. The molar concentration of  $\text{Na}_2\text{S}_6$  in both solutions was controlled at around 15 mM. Then the solutions were left to stand for 24 h to conduct adsorption experiments. After adsorption, we took out a portion of the supernatant and diluted it for testing by UV-vis examinations, and the color was observed by digital photographs.

### 3. Results and Discussion

#### 3.1. Characterization of $\text{Na}_2\text{S}-\text{Na}_6\text{CoS}_4/\text{Co}@C$ and $\text{Na}_2\text{S}@C$

Figure 1 is the schematic illustration of the synthesis procedure of  $\text{Na}_2\text{S}-\text{Na}_6\text{CoS}_4/\text{Co}@C$  composite using  $\text{Na}_2\text{SO}_4$ ,  $\text{CoSO}_4$ , KB, and polyvinylpyrrolidone (PVP) [29]. Through the stirring and ultrasonication treatment, a uniform mixture of  $\text{Na}_2\text{SO}_4$ ,  $\text{CoSO}_4$ , KB, and PVP in ethanol was obtained. Subsequently, the mixture was carbothermally reduced at  $900^\circ\text{C}$  under Ar flow after the ethanol was completely evaporated and the dried sample was ground. The formation of sulfides via the carbothermal reduction of sulfates has been adopted in the Leblanc process, representing an early industrial process [30–33]. This reaction, as seen in Equations (1)–(3), is expected to consume carbon and simultaneously produce some void space [34,35]. The  $\text{Na}_2\text{S}@C$  composite was synthesized through a similar process as for  $\text{Na}_2\text{S}-\text{Na}_6\text{CoS}_4/\text{Co}@C$  except with the absence of  $\text{CoSO}_4\cdot 7\text{H}_2\text{O}$ .

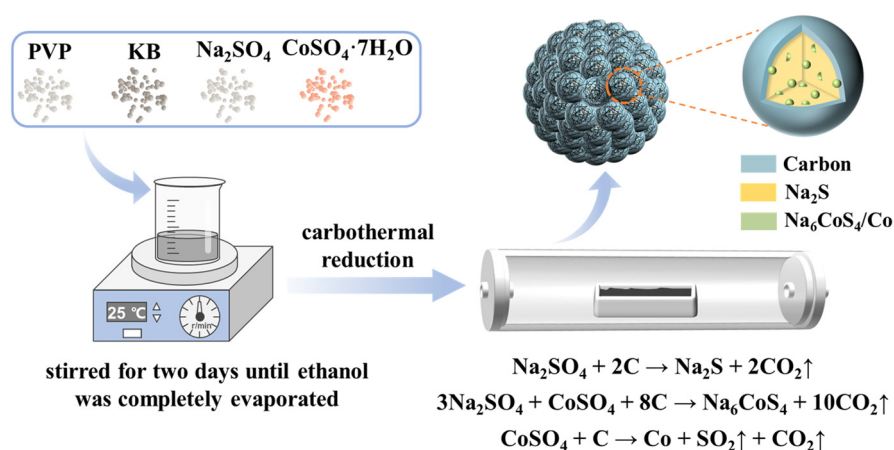
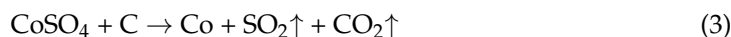
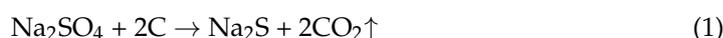


**Figure 1.** Scheme of the synthetic strategy for  $\text{Na}_2\text{S}-\text{Na}_6\text{CoS}_4/\text{Co}@C$ .

The morphology of the as-prepared  $\text{Na}_2\text{S}@C$  and  $\text{Na}_2\text{S}-\text{Na}_6\text{CoS}_4/\text{Co}@C$  composite is shown in Figure 2a–f. It is found that both composites are composed of nanoparticles interconnected to form a three-dimensional porous network and are composed of nanoparticles clustered in secondary particles of approximately 50 nm in size. The three-dimensional porous network is beneficial for electrolyte infiltration and accommodation of volume change. The high-resolution TEM (HRTEM) image of  $\text{Na}_2\text{S}@C$  in Figure 2g

confirms that the lattice fringes of crystalline nanoparticles match well with cubic  $\text{Na}_2\text{S}$  and reveals that a carbon layer in thickness of  $\approx 7.6$  nm coats with the nanoparticle. The HRTEM image of  $\text{Na}_2\text{S}\text{-Na}_6\text{CoS}_4/\text{Co}@C$  in Figure 2h,i clearly displays lattice fringes of 0.187 nm, 0.244 nm, and 0.276 nm, associated with the  $\text{Na}_2\text{S}$  (222) plane and the  $\text{Na}_6\text{CoS}_4$  (301) and (112) planes, showing that the  $\text{Na}_2\text{S}$  and  $\text{Na}_6\text{CoS}_4$  are highly crystalline. The energy-dispersive X-ray (EDX) elemental mapping of  $\text{Na}_2\text{S}@C$  and  $\text{Na}_2\text{S}\text{-Na}_6\text{CoS}_4/\text{Co}@C$  (Figure S1 and Figure S2, respectively), confirms the existence and the uniform distribution of carbon, oxygen, sodium, sulfur, and cobalt. The O content measured in the EDX elemental mapping may come from the short air contact with the samples during the transfer process to the EDX chamber [26].

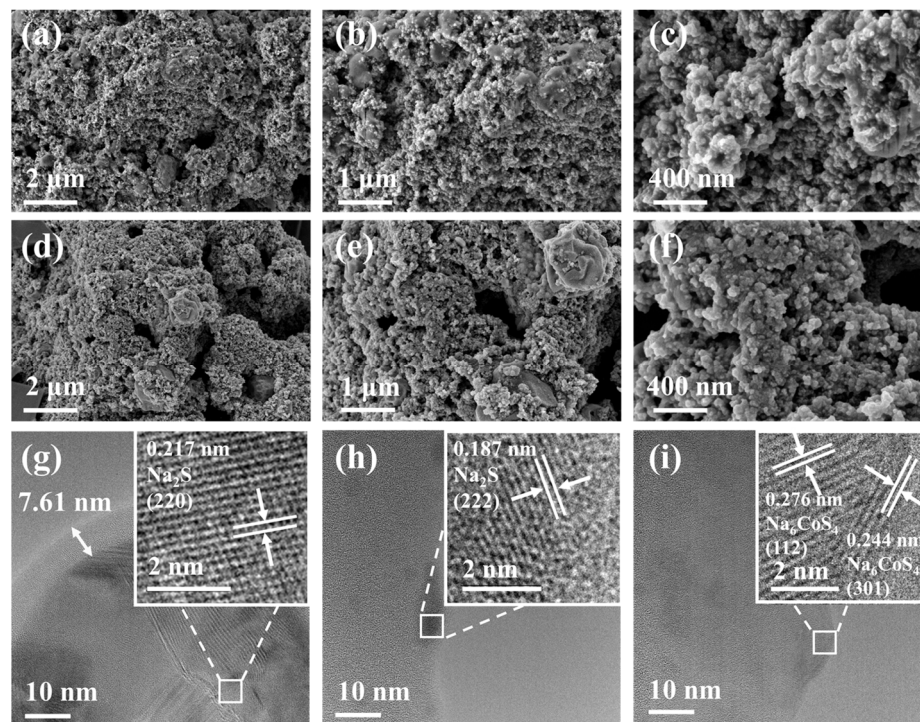


**Figure 2.** SEM of (a–c)  $\text{Na}_2\text{S}@C$  and (d–f)  $\text{Na}_2\text{S}\text{-Na}_6\text{CoS}_4/\text{Co}@C$  at various magnifications. HRTEM of (g)  $\text{Na}_2\text{S}@C$  and (h,i)  $\text{Na}_2\text{S}\text{-Na}_6\text{CoS}_4/\text{Co}@C$ .

The composition of the as-synthesized  $\text{Na}_2\text{S}@C$  and  $\text{Na}_2\text{S}\text{-Na}_6\text{CoS}_4/\text{Co}@C$  was also investigated via X-ray diffraction (XRD) measurements. In the XRD of the composites  $\text{Na}_2\text{S}@C$  and  $\text{Na}_2\text{S}\text{-Na}_6\text{CoS}_4/\text{Co}@C$  (Figure 3a,b), no  $\text{Na}_2\text{SO}_4$  peaks were detected while the  $\text{Na}_2\text{S}$  peaks (PDF#23-0441) appeared. Additionally, in the XRD pattern of the  $\text{Na}_2\text{S}\text{-Na}_6\text{CoS}_4/\text{Co}@C$ , the peaks of  $\text{Na}_6\text{CoS}_4$  (PDF#76-2173) and Co (PDF#15-0806) were also clearly detected. In Figure 3c, the intensity ratio between D ( $1341\text{ cm}^{-1}$ ) and G ( $1593\text{ cm}^{-1}$ ) band of carbon ( $I_D/I_G$ ) is 1.69, confirming the successful formation of disordered carbon in  $\text{Na}_2\text{S}@C$ . And the characteristic peaks of  $\text{Na}_2\text{S}$  (at  $446\text{ cm}^{-1}$ ) was detected by Raman spectra throughout the composite, providing the solid evidence of the uniform distribution of  $\text{Na}_2\text{S}$  in the material [36]. The  $\text{N}_2$  adsorption–desorption isotherms of the as-prepared samples are shown in Figures 3d and S3a, which both show typical features of type IV nitrogen adsorption–desorption isotherm, implying the formation of mesoporous structures in the sample. The specific surface area of both samples is calculated using the BET method. The  $\text{Na}_2\text{S}@C$  has a specific surface area of  $46.41\text{ m}^2\text{ g}^{-1}$ , higher than  $\text{Na}_2\text{S}\text{-Na}_6\text{CoS}_4/\text{Co}@C$  ( $44.76\text{ m}^2\text{ g}^{-1}$ ), suggesting the introduction of  $\text{Na}_6\text{CoS}_4/\text{Co}$  will reduce the specific surface area to some extent. Pore size distributions are also calculated using the BJH method (Figures 3e and S3b). The pore size distribution provides the evidence of the porous

structure with the average pore size being  $<10$  nm in both samples, suggesting the formation of mesoporous structures in both samples again. The large BET and mesoporous structures are beneficial for electrolyte infiltration. The surface chemical composition and electronic states of  $\text{Na}_2\text{S}-\text{Na}_6\text{CoS}_4/\text{Co}@C$  were analyzed by X-ray photoelectron spectroscopy (XPS) spectrum. The presence of sodium elements is observed by the peaks at a binding energy of 1072.2 eV in the XPS spectrum (Figure 3g) [28]. In Figure 3h, XPS spectrum of Co 2p profiles characteristic peaks of Co 2p<sub>3/2</sub> and Co 2p<sub>1/2</sub>, in which the peaks at 779.95 and 794.64 eV are associated with metallic Co, whereas the peaks at 783.70 and 798.39 eV are associated with the Co–S bond [34,37–40]. As demonstrated in Figure 3i, there are two peaks in the S 2p spectrum at 162.06 and 164.13 eV, assigning to the Na–S bond and Co–S bond [34,37], respectively. Therefore, the XRD, Raman spectra, and BET, together with the XPS results, proved the successful synthesis of  $\text{Na}_2\text{S}@C$  and  $\text{Na}_2\text{S}-\text{Na}_6\text{CoS}_4/\text{Co}@C$ .

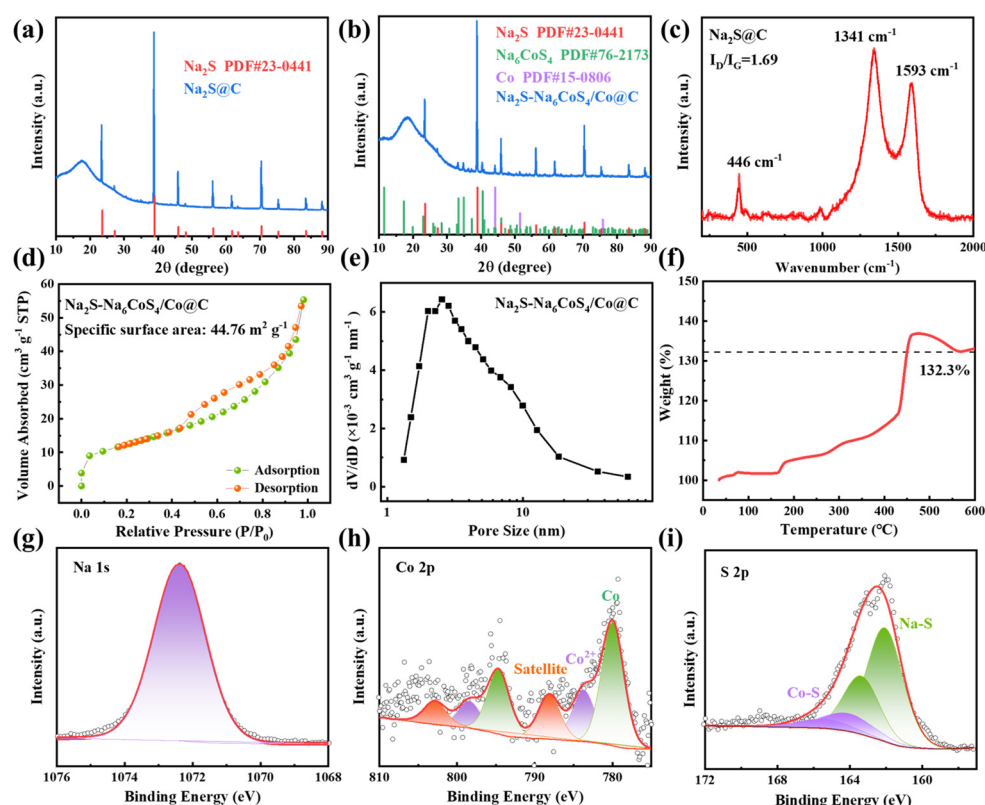


**Figure 3.** XRD of (a)  $\text{Na}_2\text{S}@C$  and (b)  $\text{Na}_2\text{S}-\text{Na}_6\text{CoS}_4/\text{Co}@C$ . (c) Raman spectra of  $\text{Na}_2\text{S}@C$ . (d)  $\text{N}_2$  adsorption–desorption isotherm of  $\text{Na}_2\text{S}-\text{Na}_6\text{CoS}_4/\text{Co}@C$ . (e) Pore size distribution of  $\text{Na}_2\text{S}-\text{Na}_6\text{CoS}_4/\text{Co}@C$ . (f) TGA curve of  $\text{Na}_2\text{S}@C$ , which is measured in dry air at a ramp rate of  $10\text{ }^{\circ}\text{C min}^{-1}$ . XPS plots of the (g) Na 1s, (h) Co 2p, and (i) S 2p regions in  $\text{Na}_2\text{S}-\text{Na}_6\text{CoS}_4/\text{Co}@C$ .

### 3.2. Investigate of $\text{Na}_2\text{S}$ Ratio in the Composites

The  $\text{Na}_2\text{S}$  ratio in the composites was investigated by two different methods acquired from the literatures. One method was based on the EDX spectra of the composites and the other was measured on thermogravimetric analysis (TGA). For the first method, the EDX spectra from three different spots of the composite were probed and then the resulted mass percentages of the  $\text{Na}_2\text{S}$  in the composites were in an average value (Table 1). Within this approach, the calculated  $\text{Na}_2\text{S}$  percentage for the composite  $\text{Na}_2\text{S}@C$  showed a value of 69.20 wt.%. It is noticed that the Na–S ratio dose not match the stoichiometry of  $\text{Na}_2\text{S}$ , staying at values less than 2 Na per S. This is in consistent with our observation that there was some metallic coating in the quartz furnace tube after carbothermal reduction. There

can be a small amount of Na metal evaporating during the high temperature treatment, and thus generating the sodium-deficient  $\text{Na}_x\text{S}$  species in the composite [26].

**Table 1.** Mass percentages of the elements C, O, Na, and S measured via EDX spectra mass analysis. For obtaining the calculated  $\text{Na}_2\text{S}$  mass contents, we left out the O content measured, as this depended on the short air contact of the samples while transferring them into the EDX chamber. Calculated values for the  $\text{Na}_2\text{S}$  ratio of the composites from EDX results and Na–S atomic ratio are presented in the table.

$\text{Na}_2\text{S}@C$	C	O	Na	S	Content of $\text{Na}_2\text{S}$	Na–S Ratio
Spot 1	21.73	28.78	26.57	22.92	69.49	1.62
Spot 2	19.53	26.14	29.76	24.57	73.55	1.69
Spot 3	24.98	29.53	26.29	19.20	64.55	1.91

To verify the previous calculations based on EDX measurements, the thermogravimetric analysis was performed at a heating ramp rate of  $10\text{ }^\circ\text{C min}^{-1}$  from room temperature to  $600\text{ }^\circ\text{C}$  in dry air. The content of  $\text{Na}_2\text{S}$  could be calculated according to Equation (4), where 78.04 and 142.04 are the molecular weights of  $\text{Na}_2\text{S}$  and  $\text{Na}_2\text{SO}_4$ , respectively, “X” (wt%) is the content of  $\text{Na}_2\text{S}$  in  $\text{Na}_2\text{S}@C$ , “ $m_1$ ”, and “ $m_2$ ” are the mass of  $\text{Na}_2\text{S}@C$  after and before high-temperature treatment, respectively. It can be obtained by TGA in Figure 3f that  $m_1:m_2 = 132.3:100$ . By substituting the above formula, the  $\text{Na}_2\text{S}$  content in the  $\text{Na}_2\text{S}@C$  composite material is calculated to be 72.69% [27]. It is obvious that based on both EDX and TGA methods, the resultant  $\text{Na}_2\text{S}$  contents in composite materials are around 70%, which are in the theoretical calculation range of 60.5 wt.% and 75.8wt.% (Supporting Information) [26]. Hence, for simplification, all electrochemical measurements were calculated based on the sulfur content according to the  $\text{Na}_2\text{S}$  ratio in the composites (70%).

$$x\% = \frac{78.04 * m_1}{142.04 * m_2} \times 100 \quad (4)$$

### 3.3. Electrochemical Performance of $\text{Na}_2\text{S}-\text{Na}_6\text{CoS}_4/\text{Co}@C$ and $\text{Na}_2\text{S}@C$

The as-prepared composite materials were assembled in coin cells and investigated their electrochemical performance. Figure 4a shows the typical galvanostatic discharge–charge voltage profiles of RT Na–S batteries based on  $\text{Na}_2\text{S}@C$  and  $\text{Na}_2\text{S}-\text{Na}_6\text{CoS}_4/\text{Co}@C$  cathodes. The increased discharge capacity, enhanced coulombic efficiency, and reduced overpotential can be observed in  $\text{Na}_2\text{S}-\text{Na}_6\text{CoS}_4/\text{Co}@C$  cells, benefiting from the efficient catalysis of  $\text{Na}_6\text{CoS}_4/\text{Co}$  composites. Three obvious reduction peaks at 2.3 V, 1.9 V, and 1.69 V for  $\text{Na}_2\text{S}@C$  (2.26 V, 1.7 V, and 1.38 V for  $\text{Na}_2\text{S}-\text{Na}_6\text{CoS}_4/\text{Co}@C$ ) are observed. The first voltage plateau ( $\sim 2.3$  V) in the discharge profile corresponds to the transition of elemental sulfur to soluble long-chain sodium polysulfides ( $\text{Na}_2\text{S}_n, 4 \leq n \leq 8$ ). The second voltage plateau is attributed to the transition of  $\text{Na}_2\text{S}_n$  ( $4 \leq n \leq 8$ ) to  $\text{Na}_2\text{S}_3$ . The third voltage plateau refers to the further transition from  $\text{Na}_2\text{S}_3$  to  $\text{Na}_2\text{S}_2$  and  $\text{Na}_2\text{S}$  [24,41–43]. The reaction route of  $\text{Na}_2\text{S}-\text{Na}_6\text{CoS}_4/\text{Co}@C$  electrodes toward sodium storage is also investigated by cyclic voltammetry (CV) tests at a scan rate of  $0.1\text{ mV s}^{-1}$  between 0.5 and 3.0 V (Figure 4b). Two obvious reduction peaks at  $\approx 1.38$  V and  $\approx 1.85$  V, along with one shoulder at  $\approx 2.25$  V and one oxidation peak centered at  $\approx 2.14$  V are observed, which are consistent with the galvanostatic discharge–charge voltage profiles.

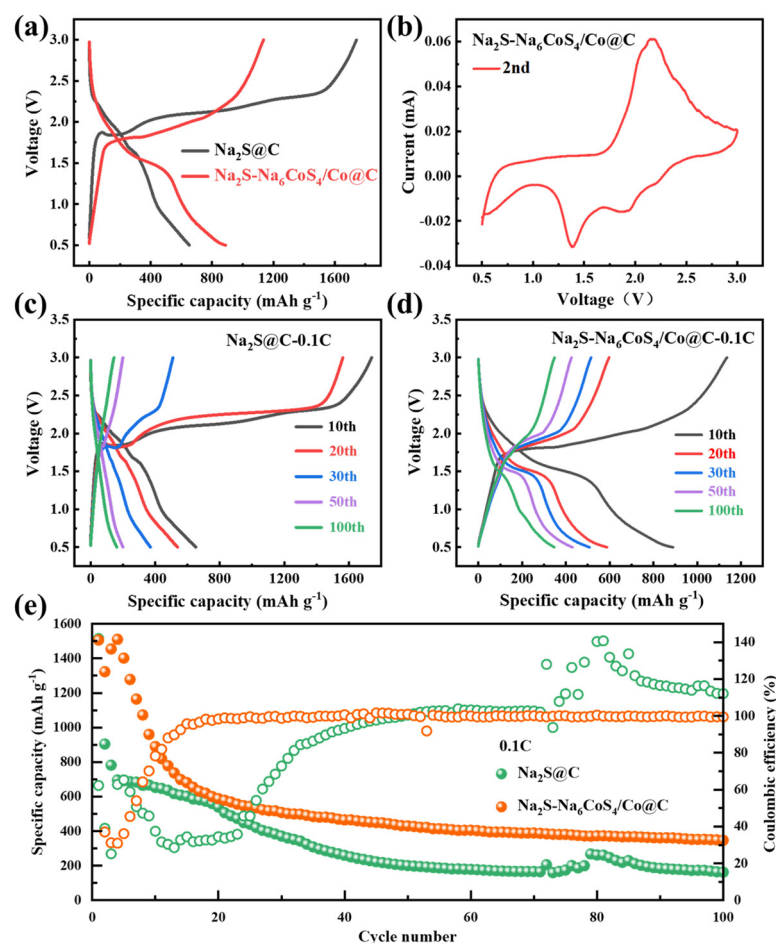


**Figure 4.** (a) Typical charge/discharge curves of the cells with Na<sub>2</sub>S@C and Na<sub>2</sub>S–Na<sub>6</sub>CoS<sub>4</sub>/Co@C cathodes at 0.1C. (b) Cyclic voltammograms of Na<sub>2</sub>S–Na<sub>6</sub>CoS<sub>4</sub>/Co@C electrode at 0.1 mV s<sup>-1</sup>. GCD profiles after different cycling stages at 0.1C of (c) Na<sub>2</sub>S@C and (d) Na<sub>2</sub>S–Na<sub>6</sub>CoS<sub>4</sub>/Co@C. (e) Cycling stability of Na<sub>2</sub>S@C and Na<sub>2</sub>S–Na<sub>6</sub>CoS<sub>4</sub>/Co@C at 0.1C rate.

The galvanostatic discharge–charge curves of Na<sub>2</sub>S@C and Na<sub>2</sub>S–Na<sub>6</sub>CoS<sub>4</sub>/Co@C cathode at the 10th, 20th, 30th, 50th, and 100th cycles are also shown in Figure 4c and Figure 4d, respectively. The good reversibility of the Na<sub>2</sub>S–Na<sub>6</sub>CoS<sub>4</sub>/Co@C cathode can be revealed by the consistency of the discharge plateaus. To testify to the long-term cycling stability, the cycling performances at 0.1 C and 0.3 C were tested, as shown in Figure 4e and Figure S4, respectively. The cell based on the Na<sub>2</sub>S@C cathode delivers a specific capacity of 1514 mAh g<sup>-1</sup> at 0.1 C initially, followed by a fast decay to 904 mAh g<sup>-1</sup> in the second cycle. Subsequently, the capacity continued to decline sharply until the 20th cycle. After 100 cycles, it remains the discharge capacity of a mere 162 mAh g<sup>-1</sup>. But for the Na<sub>2</sub>S–Na<sub>6</sub>CoS<sub>4</sub>/Co@C cathode at 0.1 C, the initial discharge capacity of 1506 mAh g<sup>-1</sup> can be delivered, and a specific capacity of up to 346 mAh g<sup>-1</sup> is still maintained after 100 cycles. When the rate further increases to 0.3 C, the capacity of Na<sub>2</sub>S–Na<sub>6</sub>CoS<sub>4</sub>/Co@C cathode can maintain at 298 mAh g<sup>-1</sup> after 100 cycles. It is also noted that the Na<sub>2</sub>S@C cathode exhibits much less stable Coulombic efficiency than that of the Na<sub>2</sub>S–Na<sub>6</sub>CoS<sub>4</sub>/Co@C composite cathode. The Na<sub>2</sub>S–Na<sub>6</sub>CoS<sub>4</sub>/Co@C cathode delivers excellent cycling stability and stable Coulombic efficiency compared with Na<sub>2</sub>S@C, suggesting its fast reaction kinetics and effective mitigation of NaPS shuttling. A comparison of the Na<sub>2</sub>S–Na<sub>6</sub>CoS<sub>4</sub>/Co@C cathode with reported Na<sub>2</sub>S–based cathodes in terms of electrochemical performance is summarized in Table S2.

Additionally, electrochemical impedance spectroscopy (EIS) measurements were conducted to compare the electrochemical kinetics of the  $\text{Na}_2\text{S}-\text{Na}_6\text{CoS}_4/\text{Co@C}$  and  $\text{Na}_2\text{S}$  cathodes, and the results are shown in Figure S5 and Table S1. The high-frequency region of the EIS results is dominated by solution resistance and small-scale charge transfer resistance, while the medium frequency is primarily related to charge transfer resistance ( $R_{ct}$ ) and kinetics of electrochemical reactions at the interface. Figure S5 and Table S1 show that the  $R_{ct}$  for the  $\text{Na}_2\text{S}-\text{Na}_6\text{CoS}_4/\text{Co@C}$  cathode is lower compared to  $\text{Na}_2\text{S@C}$  cathode, suggesting that the enhanced electronic conductivity and fast reaction kinetics in the  $\text{Na}_2\text{S}-\text{Na}_6\text{CoS}_4/\text{Co@C}$  cathode.

### 3.4. Absorptivity Measurements

To further evaluate the effectiveness of  $\text{Na}_6\text{CoS}_4/\text{Co@C}$  and C for  $\text{Na}_2\text{S}_6$  adsorption,  $\text{Na}_2\text{S}_6$  solutions containing  $\text{Na}_6\text{CoS}_4/\text{Co@C}$  or C were prepared by dispersing  $\text{Na}_2\text{S}-\text{Na}_6\text{CoS}_4/\text{Co@C}$  or  $\text{Na}_2\text{S@C}$  and S (molar ratio 1:5) into DIGLYME at  $60^\circ\text{C}$  under vigorous agitation overnight. After adsorption, a portion of the supernatant from both solutions was collected and diluted. The solution with  $\text{Na}_6\text{CoS}_4/\text{Co@C}$  displayed a lighter color compared to the one with C alone (Figure 5a), suggesting that  $\text{Na}_6\text{CoS}_4/\text{Co}$  enhances the adsorption capacity for NaPSs. The characteristic adsorption peak at 280 nm, corresponding to  $\text{S}_6^{2-}$  in UV-vis spectrometry [28], was observed. The major peak intensity decreased more significantly in the  $\text{Na}_6\text{CoS}_4/\text{Co@C}$  solution, indicating a lower residual concentration of NaPSs in the supernatant, thus confirming that  $\text{Na}_6\text{CoS}_4/\text{Co@C}$  exhibits superior adsorption ability compared to C.

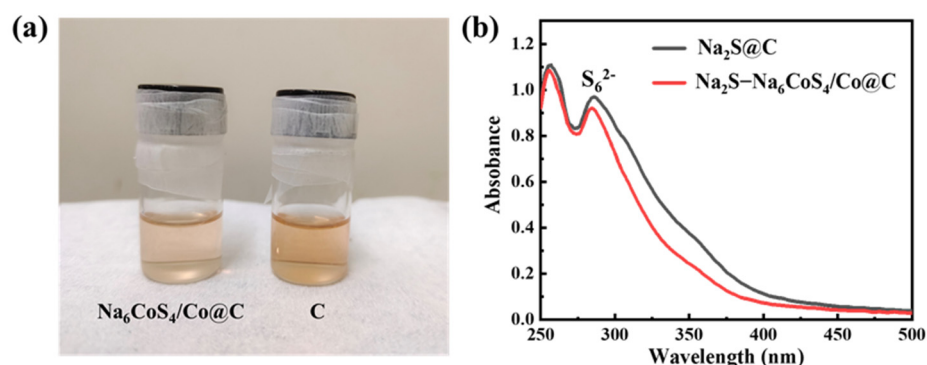


**Figure 5.** (a) Digital photos and (b) UV-vis adsorption spectra of  $\text{Na}_2\text{S}_6$  solutions trapped by  $\text{Na}_6\text{CoS}_4/\text{Co@C}$  and C.

## 4. Conclusions

In summary, a  $\text{Na}_2\text{S}$  cathode embedded in a carbon matrix and decorated with dual catalysts,  $\text{Na}_6\text{CoS}_4$  and Co ( $\text{Na}_2\text{S}-\text{Na}_6\text{CoS}_4/\text{Co@C}$ ), was synthesized via a simple carbothermal reduction of  $\text{CoSO}_4$  and  $\text{Na}_2\text{SO}_4$ . The resulting  $\text{Na}_2\text{S}-\text{Na}_6\text{CoS}_4/\text{Co}$  cathode consists of ultrafine nanoparticles, only a few nanometers in size, which form a three-dimensional porous network. This structure enhances electrolyte infiltration, while the interconnected carbon matrix facilitates continuous electron flow during electrochemical reactions. The close integration of  $\text{Na}_6\text{CoS}_4$  and Co electrocatalysts with  $\text{Na}_2\text{S}$  provides abundant catalytic activity and strong physicochemical immobilization, accelerating redox kinetics and mitigating polysulfide shuttling. At a current density of 0.1 C, both  $\text{Na}_2\text{S@C}$  and  $\text{Na}_2\text{S}-\text{Na}_6\text{CoS}_4/\text{Co@C}$  cathodes initially achieved similar discharge capacities of  $1514 \text{ mAh g}^{-1}$  and  $1506 \text{ mAh g}^{-1}$ , respectively. However, after 100 cycles, the  $\text{Na}_2\text{S}-\text{Na}_6\text{CoS}_4/\text{Co@C}$  cathode demonstrated substantially better capacity retention, with a discharge capacity of  $346 \text{ mAh g}^{-1}$ , whereas the  $\text{Na}_2\text{S@C}$  cathode exhibited a notable capacity loss. These results highlight the critical role of catalyst integration within  $\text{Na}_2\text{S}$  cathodes for high-

performance room-temperature Na–S batteries, providing a promising strategy for the design of Na<sub>2</sub>S–based cathodes with embedded catalysts.

**Supplementary Materials:** The following supporting information can be downloaded at: <https://www.mdpi.com/article/10.3390/batteries11010009/s1>, Figure S1: SEM images and corresponding elemental mapping of Na<sub>2</sub>S@C.; Figure S2: SEM images and corresponding elemental mapping of Na<sub>2</sub>S–Na<sub>6</sub>CoS<sub>4</sub>/Co@C; Figure S3: (a) N<sub>2</sub> adsorption–desorption isotherm of Na<sub>2</sub>S@C. (b) Pore size distribution of Na<sub>2</sub>S@C. Figure S4. Cycling stability of Na<sub>2</sub>S@C and Na<sub>2</sub>S–Na<sub>6</sub>CoS<sub>4</sub>/Co@C at 0.3 C rate. Figure S5. EIS analysis of Na<sub>2</sub>S@C and Na<sub>2</sub>S–Na<sub>6</sub>CoS<sub>4</sub>/Co@C after 100 cycles. Table S1. Impedance parameters for Na<sub>2</sub>S–Na<sub>6</sub>CoS<sub>4</sub>/Co@C and Na<sub>2</sub>S@C cathodes after 100 cycles state simulated from the equivalent circuits. Table S2. A comparison of Na<sub>2</sub>S–Na<sub>6</sub>CoS<sub>4</sub>/Co@C cathode with reported Na<sub>2</sub>S-based cathodes in electrochemical performance. Reference [44] is cited in the supplementary materials.

**Author Contributions:** S.M.: Methodology, Investigation, Writing—original draft. Y.Z.: Resources, Investigation. Y.Y.: Resources. D.L.: Resources. W.T.: Resources, Supervision. L.G.: Resources. W.Z.: Resources. W.L. (Wenbo Liu): Resources, Supervision. W.L. (Wenyu Liang): Resources, Writing—review and editing. R.X.: Conceptualization, Methodology, Resources, Writing—review and editing. All authors have read and agreed to the published version of the manuscript.

**Funding:** This research was funded by the National Natural Science Foundation of China, grant number No. 52102204 and the start-up research funding of the University of Science and Technology Beijing (FRF-TP-24-001A) and the Fundamental Research Funds for the Central Universities (QNXM20230009).

**Data Availability Statement:** The original contributions presented in the study are included in the article, further inquiries can be directed to the corresponding author.

**Acknowledgments:** We gratefully acknowledge the University of Science and Technology Beijing for their support with XRD, Raman, FTIR, SEM, FIB-SEM, XPS, and TEM analyses. We also extend our sincere thanks to Guangsheng Dong for his valuable discussions.

**Conflicts of Interest:** The authors declare no conflicts of interest. The funders had no role in the design of the study; in the collection, analyses, or interpretation of data; in the writing of the manuscript; or in the decision to publish the results.

## References

1. Wang, L.; Wang, H.; Zhang, S.; Ren, N.; Wu, Y.; Wu, L.; Zhou, X.; Yao, Y.; Wu, X.; Yu, Y. Manipulating the Electronic Structure of Nickel via Alloying with Iron: Toward High-Kinetics Sulfur Cathode for Na-S Batteries. *ACS Nano* **2021**, *15*, 15218–15228. [CrossRef]
2. Hong, X.; Mei, J.; Wen, L.; Tong, Y.; Vasileff, A.; Wang, L.; Laing, J.; Sun, Z.; Dou, S. Nonlithium Metal–Sulfur Batteries: Steps Toward a Leap. *Adv. Mater.* **2019**, *31*, 1802822. [CrossRef]
3. Lee, B.; Paek, E.; Mitlin, D.; Lee, S. Sodium Metal Anodes: Emerging Solutions to Dendrite Growth. *Chem. Rev.* **2019**, *119*, 5416–5460. [CrossRef]
4. Wang, Y.; Lai, W.; Chou, S.; Liu, H.; Dou, S. Remedies for Polysulfide Dissolution in Room-Temperature Sodium–Sulfur Batteries. *Adv. Mater.* **2019**, *32*, 1903952. [CrossRef]
5. Yu, X.; Manthiram, A. Capacity Enhancement and Discharge Mechanisms of Room-Temperature Sodium–Sulfur Batteries. *ChemElectroChem* **2015**, *1*, 1275–1280. [CrossRef]
6. Wang, N.; Wang, Y.; Bai, Z.; Fang, Z.; Zhang, X.; Xu, Z.; Ding, Y.; Xu, X.; Du, Y.; Dou, S.; et al. High-performance room-temperature sodium–sulfur battery enabled by electrocatalytic sodium polysulfides full conversion. *Energy Environ. Sci.* **2020**, *13*, 562–570. [CrossRef]
7. Castillo, J.; Qiao, L.; Santiago, A.; Judez, X.; Sáenz de Buruaga, A.; Jiménez-Martín, G.; Armand, M.; Zhang, H.; Li, C. Perspective of polymer-based solid-state Li-S batteries. *Energy Mater.* **2022**, *2*, 200003. [CrossRef]
8. Long, B.; Ma, J.; Song, T.; Liu, L.; Wang, X.; Song, S.; Tong, Y. Bifunctional polyvinylpyrrolidone generates sulfur-rich copolymer and acts as “residence” of polysulfide for advanced lithium-sulfur battery. *Chem. Eng. J.* **2021**, *414*, 128799. [CrossRef]

9. Lin, L.; Zhang, C.; Huang, Y.; Zhuang, Y.; Fan, M.; Lin, J.; Wang, L.; Xie, Q.; Peng, D. Challenges and Strategies for Room-Temperature Sodium-Sulfur Batteries: A Comparison with Lithium-Sulfur Batteries. *Small* **2022**, *18*, 2107368. [[CrossRef](#)]
10. Li, Y.; Wang, X.; Wang, L.; Jia, D.; Yang, Y.; Liu, X.; Sun, M.; Zhao, Z.; Qiu, J. Ni@Ni<sub>3</sub>N embedded on three-dimensional carbon nanosheets for high-performance lithium/sodium-sulfur batteries. *ACS Appl. Mater. Interfaces* **2021**, *13*, 48536–48545. [[CrossRef](#)] [[PubMed](#)]
11. Guo, B.; Du, W.; Yang, T.; Deng, J.; Liu, D.; Qi, Y.; Jiang, J.; Bao, S.; Xu, M. Nickel Hollow Spheres Concatenated by Nitrogen-Doped Carbon Fibers for Enhancing Electrochemical Kinetics of Sodium-Sulfur Batteries. *Adv. Sci.* **2019**, *7*, 1902617. [[CrossRef](#)]
12. Hao, H.; Wang, Y.; Katyal, N.; Yang, G.; Dong, H.; Liu, P.; Hwang, S.; Mantha, J.; Henkelman, G.; Xu, Y.; et al. Molybdenum Carbide Electrocatalyst In Situ Embedded in Porous Nitrogen-Rich Carbon Nanotubes Promotes Rapid Kinetics in Sodium-Metal-Sulfur Batteries. *Adv. Mater.* **2022**, *34*, 2106572. [[CrossRef](#)] [[PubMed](#)]
13. Ma, D.; Li, Y.; Yang, J.; Mi, H.; Luo, S.; Deng, L.; Yan, C.; Rauf, M.; Zhang, P.; Sun, X.; et al. New Strategy for Polysulfide Protection Based on Atomic Layer Deposition of TiO<sub>2</sub> onto Ferroelectric-Encapsulated Cathode: Toward Ultrastable Free-Standing Room Temperature Sodium–Sulfur Batteries. *Adv. Funct. Mater.* **2018**, *28*, 1705537. [[CrossRef](#)]
14. Ye, C.; Jin, H.; Shan, J.; Jiao, Y.; Li, H.; Gu, Q.; Davey, K.; Wang, H.; Qiao, S. A Mo<sub>5</sub>N<sub>6</sub> electrocatalyst for efficient Na<sub>2</sub>S electrodeposition in room-temperature sodium-sulfur batteries. *Nat. Commun.* **2021**, *12*, 7195. [[CrossRef](#)] [[PubMed](#)]
15. Zhang, B.; Sheng, T.; Liu, Y.; Wang, Y.; Zhang, L.; Lai, W.; Wang, L.; Yang, J.; Gu, Q.; Chou, S.; et al. Atomic cobalt as an efficient electrocatalyst in sulfur cathodes for superior room-temperature sodium-sulfur batteries. *Nat. Commun.* **2018**, *9*, 4082. [[CrossRef](#)]
16. Qin, G.; Liu, Y.; Han, P.; Cao, S.; Guo, X.; Guo, Z. High performance room temperature Na-S batteries based on FCNT modified Co<sub>3</sub>C-Co nanocube. *Chem. Eng. J.* **2020**, *396*, 125295. [[CrossRef](#)]
17. Yang, H.; Zhou, S.; Zhang, B.; Chu, S.; Guo, H.; Gu, Q.; Liu, H.; Lei, Y.; Konstantinov, K.; Wang, Y.; et al. Architecting Freestanding Sulfur Cathodes for Superior Room-Temperature Na-S Batteries. *Adv. Funct. Mater.* **2021**, *31*, 2102280. [[CrossRef](#)]
18. Du, W.; Shen, K.; Qi, Y.; Gao, W.; Tao, M.; Du, G.; Bao, S.; Chen, M.; Chen, Y.; Xu, M. Efficient Catalytic Conversion of Polysulfides by Biomimetic Design of “Branch-Leaf” Electrode for High-Energy Sodium–Sulfur Batteries. *Nano-Micro Lett.* **2021**, *13*, 50. [[CrossRef](#)] [[PubMed](#)]
19. Mou, J.; Li, Y.; Liu, T.; Zhang, W.; Li, M.; Xu, Y.; Zhong, L.; Pan, W.; Yang, C.; Huang, J.; et al. Metal-Organic Frameworks-Derived Nitrogen-Doped Porous Carbon Nanocubes with Embedded Cobalt Nanoparticles as High-Efficiency Sulfur Stabilizers for Room-Temperature Sodium-Sulfur Batteries. *Small Methods* **2021**, *5*, 2100455. [[CrossRef](#)]
20. Chen, P.; Wang, C.; Wang, T. Review and prospects for room-temperature sodium-sulfur batteries. *Mater. Res. Lett.* **2022**, *10*, 691–719. [[CrossRef](#)]
21. Aslam, M.; Niu, Y.; Hussain, T.; Tabassum, H.; Tang, W.; Xu, M.; Ahuja, R. How to avoid dendrite formation in metal batteries: Innovative strategies for dendrite suppression. *Nano Energy* **2021**, *86*, 106142. [[CrossRef](#)]
22. Wang, Y.; Zhou, D.; Palomares, V.; Shanmukaraj, D.; Sun, B.; Tang, X.; Wang, C.; Armand, M.; Rojo, T.; Wang, G. Revitalizing Sodium-Sulfur Batteries for Non-High-Temperature Operation: A Crucial Review. *Energy Environ. Sci.* **2020**, *13*, 3848–3879. [[CrossRef](#)]
23. Wang, C.; Wang, H.; Hu, X.; Matios, E.; Luo, J.; Zhang, Y.; Lu, X.; Li, W. Frogspawn-Coral-Like Hollow Sodium Sulfide Nanostructured Cathode for High-Rate Performance Sodium-Sulfur Batteries. *Adv. Energy Mater.* **2019**, *9*, 1803251. [[CrossRef](#)]
24. Yu, X.; Manthiram, A. Na<sub>2</sub>S–Carbon Nanotube Fabric Electrodes for Room-Temperature Sodium–Sulfur Batteries. *Chem. Eur. J.* **2015**, *21*, 4233–4237. [[CrossRef](#)] [[PubMed](#)]
25. Fan, X.; Yue, J.; Han, F.; Chen, J.; Deng, T.; Zhou, X.; Hou, S.; Wang, C. High-Performance All-Solid-State Na–S Battery Enabled by Casting–Annealing Technology. *ACS Nano* **2018**, *12*, 3360–3368. [[CrossRef](#)]
26. Bloi, L.; Pampel, J.; Dörfler, S.; Althues, H.; Kaskel, S. Sodium Sulfide Cathodes Superseding Hard Carbon Pre-sodiation for the Production and Operation of Sodium–Sulfur Batteries at Room Temperature. *Adv. Energy Mater.* **2020**, *10*, 1903245. [[CrossRef](#)]
27. Geng, M.; Han, D.; Huang, Z.; Wang, S.; Xiao, M.; Zhang, S.; Sun, L.; Huang, S.; Meng, Y. A stable anode-free Na-S full cell at room temperature. *Energy Storage Mater.* **2022**, *52*, 230–237. [[CrossRef](#)]
28. Gao, W.; Su, L.; Yu, Y.; Lu, Y.; Liu, X.; Peng, Y.; Xiong, X.; He, J.; Chen, Y.; Wu, Y. Stable Dendrite-Free Room Temperature Sodium-Sulfur Batteries Enabled by a Novel Sodium Thiotellurate Interface. *Angew. Chem. Int. Ed.* **2024**, *63*, e202412287. [[CrossRef](#)]
29. He, J.; Bhargava, A.; Manthiram, A. High-Performance Anode-Free Li–S Batteries with an Integrated Li<sub>2</sub>S–Electrocatalyst Cathode. *ACS Energy Lett.* **2022**, *7*, 583–590. [[CrossRef](#)]
30. Yuan, K.; Yuan, L.; Chen, J.; Xiang, J.; Liao, Y.; Li, Z.; Huang, Y. Methods and Cost Estimation for the Synthesis of Nanosized Lithium Sulfide. *Small Struct.* **2020**, *2*, 2000059. [[CrossRef](#)]
31. Ye, F.; Noh, H.; Lee, J.; Lee, H.; Kim, H. Li<sub>2</sub>S/carbon nanocomposite strips from a low-temperature conversion of Li<sub>2</sub>SO<sub>4</sub> as high-performance lithium–sulfur cathodes. *J. Mater. Chem. A* **2018**, *6*, 6617–6624. [[CrossRef](#)]
32. Liu, J.; Nara, H.; Yokoshima, T.; Momma, T.; Osaka, T. Micro-scale Li<sub>2</sub>S–C composite preparation from Li<sub>2</sub>SO<sub>4</sub> for cathode of lithium ion battery. *Electrochim. Acta* **2015**, *183*, 70–77. [[CrossRef](#)]

33. Yang, Z.; Guo, J.; Das, S.; Yu, Y.; Zhou, Z.; Abruñab, H.; Archer, L. In situ synthesis of lithium sulfide–carbon composites as cathode materials for rechargeable lithium batteries. *J. Mater. Chem. A* **2013**, *1*, 1433–1440. [[CrossRef](#)]
34. Yu, M.; Wang, Z.; Wang, Y.; Dong, Y.; Qiu, J. Freestanding Flexible Li<sub>2</sub>S Paper Electrode with High Mass and Capacity Loading for High-Energy Li–S Batteries. *Adv. Energy Mater.* **2017**, *7*, 1700018. [[CrossRef](#)]
35. He, J.; Bhargav, A.; Okasinski, J.; Manthiram, A. A Class of Sodium Transition-Metal Sulfide Cathodes with Anion Redox. *Adv. Mater.* **2024**, *36*, 2403521. [[CrossRef](#)]
36. Qi, Y.; Li, Q.; Wu, Y.; Bao, S.; Li, C.; Chen, Y.; Wang, G.; Xu, M. A Fe<sub>3</sub>N/carbon composite electrocatalyst for effective polysulfides regulation in room-temperature Na-S batteries. *Nat. Commun.* **2021**, *12*, 6347. [[CrossRef](#)] [[PubMed](#)]
37. Han, L.; Wu, Y.; Zhao, B.; Meng, W.; Zhang, D.; Li, M.; Pang, R.; Zhang, Y.; Cao, A.; Shang, Y. Carbon Nanotube-Coupled Seaweed-like Cobalt Sulfide as a Dual-Functional Catalyst for Overall Water Splitting. *ACS Appl. Mater. Interfaces* **2022**, *14*, 30847–30856. [[CrossRef](#)]
38. Sun, J.; Zheng, Y.; Zhang, Z.; Meng, X.; Li, Z. Modulation of d-orbital to realize enriched electronic cobalt sites in cobalt sulfide for enhanced hydrogen evolution in electrocatalytic water/seawater splitting. *Rare Met.* **2024**, *43*, 511–521. [[CrossRef](#)]
39. Zhao, Y.; Li, T.; Wang, Q.; Ai, Y.; Hou, R.; Habib, A.; Shao, G.; Wang, F.; Zhang, P. A parallel array structured cobalt sulfide/nitrogen doped carbon nanocage/carbon fiber composite based on microfluidic spinning technology: A novel design to boost overall water splitting. *J. Mater. Chem. A* **2024**, *12*, 23872–23879. [[CrossRef](#)]
40. Gao, S.; He, Y.; Li, H.; Yue, G.; Gui, Z.; Li, Y.; Bai, J.; Wang, N.; Zhang, Q.; Yu, Y.; et al. MoS<sub>2</sub>@CoS<sub>2</sub> heterostructured tube-in-tube hollow nanofibers with enhanced reaction reversibility and kinetics for sodium-ion storage. *Energy Storage Mater.* **2024**, *65*, 103170. [[CrossRef](#)]
41. Manthiram, A.; Yu, X. Ambient Temperature Sodium–Sulfur Batteries. *Small* **2015**, *11*, 2108–2114. [[CrossRef](#)] [[PubMed](#)]
42. Lei, Y.; Liu, H.; Yang, Z.; Zhao, L.; Lai, W.; Chen, M.; Liu, H.; Dou, S.; Wang, Y. A Review on the Status and Challenges of Cathodes in Room-Temperature Na–S Batteries. *Adv. Funct. Mater.* **2022**, *33*, 2212600. [[CrossRef](#)]
43. Yan, Z.; Liang, Y.; Xiao, J.; Lai, W.; Wang, W.; Xia, Q.; Wang, Y.; Gu, Q.; Lu, H.; Chou, S.; et al. A High-Kinetics Sulfur Cathode with a Highly Efficient Mechanism for Superior Room-Temperature Na–S Batteries. *Adv. Mater.* **2020**, *32*, 1906700. [[CrossRef](#)]
44. Kohl, M.; Brückner, J.; Bauer, I.; Althuesa, H.; Kaskel, S. Synthesis of highly electrochemically active Li<sub>2</sub>S nanoparticles for lithium–sulfur-batteries. *J. Mater. Chem. A* **2015**, *3*, 16307–16312. [[CrossRef](#)]

**Disclaimer/Publisher’s Note:** The statements, opinions and data contained in all publications are solely those of the individual author(s) and contributor(s) and not of MDPI and/or the editor(s). MDPI and/or the editor(s) disclaim responsibility for any injury to people or property resulting from any ideas, methods, instructions or products referred to in the content.